IEEE Open Journal of Signal Processing

Received 1 April 2024; revised 25 July 2024; accepted 29 July 2024. Date of publication 15 August 2024;
date of current version 20 September 2024. The review of this article was arranged by Associate Editor C. Masouros.

Digital Object Identifier 10.1109/OJSP.2024.3444709

Occlusion-Informed Radar Detection for Millimeter-Wave Indoor Sensing

AHMED MURTADA [1] (Member, IEEE), BHAVANI SHANKAR MYSORE RAMA RAO [1] (Senior Member, IEEE), MOEIN AHMADI [1] (Member, IEEE), AND UDO SCHROEDER [2]

[1]Interdisciplinary Centre for Security, Reliability and Trust (SnT), University of Luxembourg, L-1885 Luxembourg City, Luxembourg
[2]IEE S.A., L-7795 Bissen, Luxembourg

CORRESPONDING AUTHOR: AHMED MURTADA (e-mail: ahmed.murtada@uni.lu).

This work was supported by Luxembourg National Research Fund (FNR) under Grant IF/15364040/RADII.

ABSTRACT The emergence of Multiple-Input Multiple-Output (MIMO) millimeter-wave (mmWave) radar sensors has prompted interest in indoor sensing applications, including human detection, vital signs monitoring, and real-time tracking in crowded environments. These sensors, equipped with multiple antenna elements, offer high angular resolution, often referred to as imaging radars for their capability to detect high-resolution point clouds. Employing radar systems with high-angular resolution in occlusion-prone scenarios often results in sparse signal returns in range profiles. In extreme cases, only one target return may be observed, as the resolution grid size becomes significantly smaller than the targets, causing portions of the targets to consistently occupy the full area of a test cell. Leveraging this structure, we propose two detectors to enhance the detection of non-occluded targets in such scenarios, thereby providing accurate high-resolution point clouds. The first method employs multiple hypothesis testing over each range profile where the range cells within are considered mutually occluding. The second is formulated based on binary hypothesis testing for each cell, considering the distribution of the signal in the other cells within the same range profile. Numerical analysis demonstrates the superior performance of the latter method over both the classic detection and the former method, especially in low Signal-to-Noise Ratio (SNR) scenarios. Our work showcases the potential of occlusion-informed detection in imaging radars to improve the detection probability of non-occluded targets and reduce false alarms in challenging indoor environments.

INDEX TERMS Millimeter-wave radar, MIMO sensors, occlusion-informed, detection, indoor sensing, hypothesis testing.

I. INTRODUCTION

Over the past few years, there has been a surge of interest in mmWave MIMO radar sensors, especially for their applications in indoor sensing. These applications include tasks such as human detection and activity recognition, monitoring vital signs, fall detection, and real-time tracking of multiple individuals simultaneously, as demonstrated in [1], [2], [3], and [4], respectively. Advancements in mmWave sensor manufacturing technology have made such tasks possible. This development has led to the production of affordable single-chip radar sensors incorporating a large number of antenna elements, facilitating high angular resolution and resulting in the emergence of a category of imaging radars (see, for example, [5], [6]). Moreover, the optimization of various MIMO waveforms has enabled the attainment of enhanced angular performance which is an essential feature for many of the aforementioned tasks. Examples of different proposed MIMO waveforms are presented in [7], [8], [9], [10].

When monitoring human targets in indoor environments, the detection performance, preferably of the full body, holds paramount importance for various applications. However, in typical crowded indoor settings, the likelihood of occluding human targets or substantial portions of their bodies is quite high, posing a significant challenge for achieving satisfactory performance across all these applications [11], [12], [13], [14].

In the realm of automotive perception, occlusion remedies involve multi-modal fusion, where occlusion scenarios

are modeled by combining radar measurements with other sensors like stereo cameras, as seen in [15], or LIDAR, as demonstrated in [16]. On the other hand, within indoor applications, several studies have proposed distributed radar sensor architectures that enhance detection capabilities of occluded targets significantly through the exploitation of spatial diversity [17], [18], [19], [20].

While distributed sensors are essential to detect occluded targets, further measures can be taken to combat occlusion. In the context of tracking multiple individuals with distributed sensors, occlusion events concerning one sensor can lead to the division of a single track into multiple tracks. A solution, proposed in [21], [22], involves overcoming this issue by fusing track information instead of detection points in the fusion center. On another note, to better account for the capture of the Doppler falling signatures, while limiting occlusion events, the authors in [23] analyzed different sensor placements and showed that wall-mounting of distributed sensors at a low level is favorable to optimize the extraction of both range and micro-Doppler information necessary to detect falling events. While the placement of sensors to minimize occlusion is also considered by the authors in [11], their proposed gait recognition classifier is adjusted to make decisions based on features expected to be least affected by the occlusion. Similarly, in [12], the authors employed an architecture featuring separate transmitting and receiving antennas for vital sign monitoring. Using this bi-static setup, they determined the angular and distance separation of multiple targets to minimize mutual occlusion, resulting in effective vital sign monitoring with the transmission of a single beam or steered multiple beams.

The studies mentioned above effectively tackle detection limitations arising from occlusion and propose methods to generate high-resolution detection point clouds. However, to the best of the authors' knowledge, no study explicitly leverages the structure of individual range profile signals under occlusion in the hypothesis testing formulation of the detection problem. This structure is inherently sparse–particularly when utilizing high-angular resolution systems–and incorporating it could significantly enhance the detection capabilities of non-occluded targets, as occlusion would be evident across each angular bin of the test grid. A significant body of literature exists on exploiting scene sparsity in radar image reconstruction (see, for example, [24], [25], [26], [27], [28], [29], [30], [31]), which is often motivated by the typical low number of targets in the scene in addition to the properties of electromagnetic backscattering, including occlusion phenomenon [24], [26]. However, these methods rely on compressive sensing theory and involve solving inverse problems which usually require hyperparameter tuning and lead to iterative algorithms that are computationally and time expensive, rendering them unsuitable for real-time applications in many cases [32].

In this paper, we demonstrate that leveraging the sparse structure in a hypothesis testing-based formulation provides a statistical detector that enhances the detection performance for non-occluded targets observed by a single sensor, resulting in accurate high-resolution point clouds. This improved detection at the sensor level would aggregate across a network of sensors, leading to an overall enhancement in detection at a low computational cost. We capitalize on the phenomenon that in a sensing system susceptible to occlusion, conducting detection over a dense angular grid yields limited return responses across multiple range cells within the same angular bin. Consequently, we design detectors to enhance the probability of detection versus false alarms for fully observed target areas. These detectors assume complete occupancy of an angular resolution cell, implying full occlusion of any potential object behind the occupied cell within each range profile. This assumption can be justified considering system parameters, as will be demonstrated in Section II.

Accordingly, leveraging the sparse structure of range profiles, we introduce two detectors based on distinct formulations of hypothesis testing. The first approach utilizes multiple hypothesis testing, framing the detection problem to closely match the full occlusion scenario. This involves deciding that the presence of a target will be only in one cell of each range profile. On the other hand, the second approach is constructed using binary hypothesis testing. Here, the alternative and null hypotheses for each cell are established with consideration for the likelihood of the signal in the remaining cells within the same group of mutually occluding cells. For each of these formulations, we derive both Maximum A Posteriori (MAP) and Maximum Likelihood (ML) detectors. The MAP detector assumes prior knowledge of the probability model and values associated with targets' presence in different cells and utilizes this information in decision-making. On the other hand, the ML detector lacks such knowledge and assumes equal probabilities of targets arriving in the group of mutually occluding cells. While the multiple hypothesis formulation represents the straightforward, intuitive method, the binary formulation exhibits superior performance, as will be demonstrated in our numerical simulations. The contributions of this work are summarized as follows:

1) Identification and modeling of range profile structure under occlusion, utilizing probabilistic models of target presence within the detection grid cells.
2) Development of corresponding detectors using hypothesis testing, accommodating both the knowledge of the generating probabilistic models and the lack thereof.
3) Performance evaluation of the proposed detectors, demonstrated through Receiver Operating Characteristics (ROC) curves obtained numerically via Monte Carlo simulations. These simulations are based on signal generation according to the defined models and the detectors are evaluated versus model parameters, SNR values, and the number of cells in a range profile.
4) Evaluation of the proposed detectors on scenario-based simulated data, where a realistic indoor scenario is modeled in 3D, and the radar signal is generated using ray-tracing simulations.

Notations: Throughout the paper, lowercase bold font is used to denote vectors. $\mathbf{I}_N$ represents the identity matrix of size $N \times N$, and $\mathbf{0}_N$ is a vector of all zeros of size $N \times 1$. The

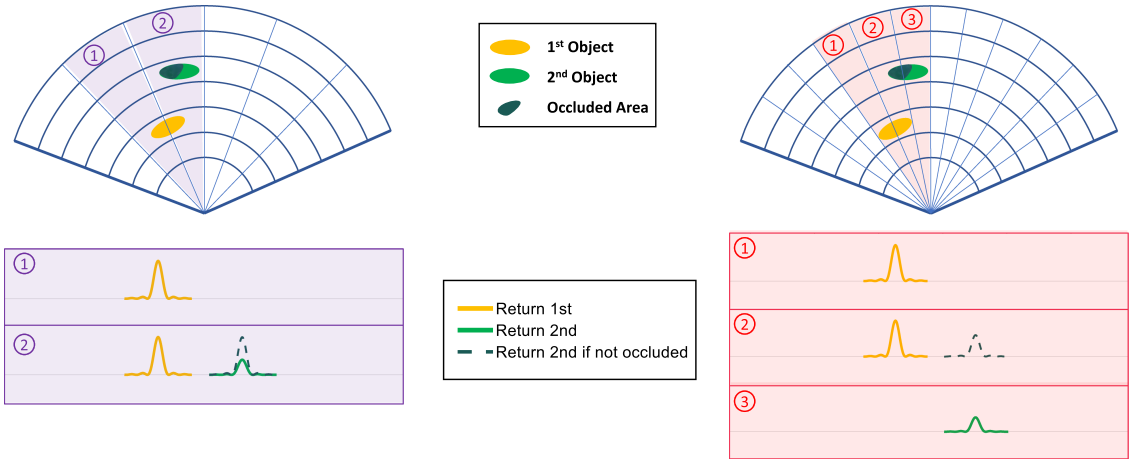

FIGURE 1. 2D Range-Azimuth grid map illustrating the sparsity of range profiles relative to targets' size in an occlusion-prone sensing environment. Two targets in the scene, with one occluding part of the other, are observed by two sensors with different angular resolutions, depicted by the corresponding angular grid sizes. Left: Sensor with low angular resolution ($\delta\theta_1$) relative to targets' size. Right: Sensor with high angular resolution ($\delta\theta_2 = 0.5\ \delta\theta_1$) relative to targets' size.

superscripts $(.)^T$ and $(.)^H$ denote, respectively, the transpose and the complex conjugate transpose of a vector or a matrix. The operators $|.|$, $\otimes$, $\Re$, and $det(.)$ are used for the absolute value operator, Kronecker product, the real part of a complex value, and the matrix determinant, respectively. With $p(x)$, we denote the probability density function of an observation x from a random variable X, where the random variable subscript is omitted for simplicity. We define the set of natural numbers from 1 to N as $\{N\} = \{1, 2, \ldots, N\}$. Accordingly, a vector with subscript $\{N\}$, e.g., $\mathbf{x}_{\{N\}}$, denotes the stacked vectors $[\mathbf{x}_1^T, \mathbf{x}_2^T, \ldots, \mathbf{x}_N^T]^T$. To shorten equations, we contract the exponential component of a Gaussian probability density function (PDF) for a random vector $\mathbf{x}$ with a mean $\boldsymbol{\mu}$ and variance σ^2 using the notation $e_{\sigma^2}(\mathbf{x}, \boldsymbol{\mu}) = \exp(\frac{-(\mathbf{x}-\mu)^H(\mathbf{x}-\mu)}{\sigma^2})$.

II. SYSTEM MODEL

In this section, we begin by demonstrating the sparsity of the range profile in high-resolution radars affected by occlusion phenomena. Next, we present the signal model and the probability of receiving backscattered returns from targets in different cells of a range profile, based on the probability of target presence in these cells.

A. OCCLUSIONS OVER RANGE PROFILES

As mentioned in the introduction, we leverage the phenomenon that in a high-angular resolution sensing system prone to occlusion, a target may fully occupy an angular resolution cell, occluding any object behind in the same range profile. Under this assumption, the processed radar signal over a dense angular grid should contain few returns across multiple range cells within the same angular bin. This behavior can be anticipated with knowledge of system parameters such as angular resolution relative to target size and transmission frequency. Fig. 1 presents a schematic illustrating the relationship between system parameters and the sparsity of range profiles in sensing under occlusion. The figure depicts a 2D elevation cut of a range-angle detection grid map from two sensors. The sensor on the right is assumed to have double the number of antenna elements, resulting in half the angular resolution compared to the sensor on the left. Both sensors observe the same scene and operate at the same frequency, indicating that the transmitted waves from both possess identical scattering/penetration characteristics. As a result, the occlusion in the scene will be consistent for both sensors. However, due to the higher angular resolution of the sensor on the right, detection tests are conducted on a finer grid. Consequently, the associated returns over a specific range profile are expected to be more sparse since targets are dispersed over more angular bins. The figure highlights the angular bins containing targets under each system, with their ideal range profiles depicted below the corresponding grid map.

The sparsity of range profiles arises from both the occlusion phenomenon and the size of the angular grid relative to the target size. If occlusion does not occur, all targets will induce a response in the range profile of each angular bin. Similarly, if the sensor's angular resolution does not permit detection cells significantly smaller than the target size, a single range profile would contain multiple responses from targets over a wider angle range, even if parts are occluded. Ultimately, when using an imaging radar, angular bins are anticipated to be fully occupied by a portion of the target at the respective location, leading to sparse range profiles, as they consist of a group of mutually occluding cells.

Similarly, Fig. 2 illustrates the same concept in an indoor scenario involving human targets, where detection is conducted over a 3D detection grid map. The figure highlights one range profile consisting of mutually occluding cells situated on the same azimuth and elevation angle. The presence of a target (or a portion thereof) in one of these cells closer to the sensor would obstruct targets that may exist in any other cell within the same group. In such instances, the reception of

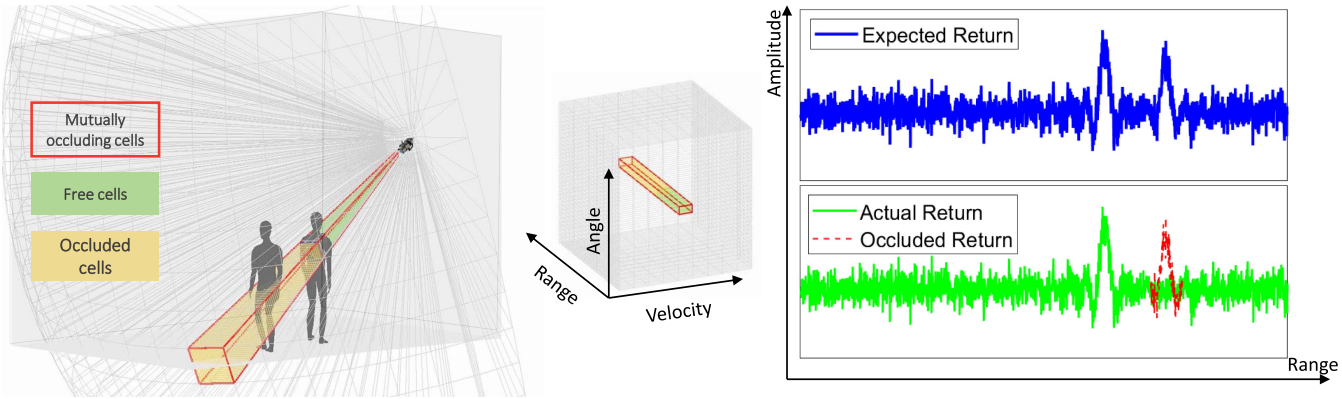

FIGURE 2. 3D Demonstration of a full occlusion scenario over a range profile in an indoor environment observed with a mmWave sensor featuring high angular resolution. **Left:** Layout of the scene with the detection grid showing the sensor's view and highlighted group of mutually occluding cells. **Middle:** Corresponding radar cube. **Right:** Expected and actual signal returns in the group of highlighted cells.

echoes of the transmitted wave from potential targets in those cells is physically impeded. This is the scenario we consider in this paper and refer to as "full occlusion" throughout the paper.

B. SIGNAL MODEL

We consider a mmWave MIMO radar sensor having N_{tx} and N_{rx} transmitting and receiving antenna elements, respectively. Assume that $\mathbf{r}_s = [x_s, y_s, z_s]^T$ denotes the absolute position of the sensor, where x, y, and z represent the absolute Cartesian coordinates. In this case, a target with absolute position $\mathbf{r}_t = [x_t, y_t, z_t]^T$ will have a relative distance R_t, azimuth θ_t, and elevation ϕ_t with respect to the sensor. Following appropriate range processing (either through fast Fourier transform (FFT) or matched filter), the target processed signal at the range cell–specifically the Cell Under Test (CUT)–corresponding to R_t can be expressed as:

$$\mathbf{x}_t = \alpha_t \mathbf{s}(\theta_t, \phi_t) + \mathbf{w} \in \mathbb{C}^{N_{tx}N_{rx}\times 1}. \tag{1}$$

Here, $\alpha_t = \sqrt{\frac{p_{tx}G_{tx}G_{rx}\lambda^2\sigma_t}{(4\pi)^3R^4}}$ represents the amplitude of the reflected signal, encompassing path loss and target Radar Cross Section (RCS), where λ denotes the transmitted signal's wavelength, p_{tx} is the transmit power, G_{tx} and G_{rx} denote the transmit and receive antenna gains, and σ_t is the RCS of the target at the CUT. Additionally, $\mathbf{w}$ denotes the receiver thermal noise, assumed to be a complex Gaussian noise $\mathbf{w} \sim \mathcal{CN}(\mathbf{0}, \sigma_{\mathbf{w}}^2\mathbf{I})$. Moreover, the signal steering vector is,

$$\mathbf{s}(\theta_t, \phi_t) = \mathbf{a}(\theta_t, \phi_t) \otimes \mathbf{b}(\theta_t, \phi_t), \tag{2}$$

where the spatial transmit and receive steering vectors are defined respectively as

$$\mathbf{a}(\theta,\phi) = \begin{bmatrix} e^{-j\mathbf{k}^T(\theta,\phi)\mathbf{r}_{s,1}} \\ e^{-j\mathbf{k}^T(\theta,\phi)\mathbf{r}_{s,2}} \\ \vdots \\ e^{-j\mathbf{k}^T(\theta,\phi)\mathbf{r}_{s,N_{tx}}} \end{bmatrix}, \mathbf{b}(\theta,\phi) = \begin{bmatrix} e^{-j\mathbf{k}^T(\theta,\phi)\mathbf{r}_{s,1}} \\ e^{-j\mathbf{k}^T(\theta,\phi)\mathbf{r}_{s,2}} \\ \vdots \\ e^{-j\mathbf{k}^T(\theta,\phi)\mathbf{r}_{s,N_{rx}}} \end{bmatrix},$$

and $\mathbf{k}(\theta,\phi) = \frac{2\pi}{\lambda}[\cos\theta\cos\phi,\ \sin\theta\cos\phi,\ \sin\phi]^T$ is the wave-number vector with λ being the wavelength of the transmitted wave, θ and ϕ are the azimuth and elevation angles, respectively, and $\mathbf{r}_{s,n_{tx}}$ and $\mathbf{r}_{s,n_{rx}}$ are the locations of the radar transmit and receive antenna elements, respectively.

Since our focus is on designing a detector for scenarios involving full occlusion, it is crucial to model the probability of signal returns at each cell under such conditions. These probabilities can be derived by establishing a probability model for the presence of targets in each cell. Consequently, we outline the essential probability components required for the subsequent formulation of the problem. We assume each range profile encompasses a group of N mutually occluding cells. We denote P_k as the probability of the presence of a target at the k^{th} cell, where $k = 1, \ldots, N$, representing the target space probability. Accordingly, the probability of having no target present at any of the N cells is given by

$$P_0 = \prod_{k=1}^{N} (1 - P_k). \tag{3}$$

Under the full occlusion assumption over a range profile, among the potential targets in the group of N cells, only one return will be reflected to the radar sensor. As a result, we can express the signal space probabilities of receiving returns at a specific cell based on the probabilities in the target space. Let ρ_k denote the probability of receiving a return from a target located at the k^{th} cell, then

$$\begin{cases} \rho_0 = P_0 \\ \rho_1 = P_1 \\ \vdots \\ \rho_k = P_k \prod_{i=1}^{i=k-1} (1 - P_i) \end{cases} \tag{4}$$

where ρ_0 represents the probability of having no return in any of the cells, and $\sum_{k=0}^{N} \rho_k = 1$. Another useful probability in subsequent calculations is the probability of having a signal return from the k^{th} cell given that a certain n^{th} cell, especially

the CUT, has no target return. Denoting this probability as $\rho_{k/\tilde{n}}$, we can compute it using Bayes' theorem

$$\rho_{k/\tilde{n}} = \frac{\rho_{\tilde{n}/k}\ \rho_k}{\rho_{\tilde{n}}} \tag{5}$$

Since $\rho_{\tilde{n}} = 1 - \rho_n$, and by occlusion assumption $\rho_{\tilde{n}/k} = 1$, the probabilities of having a signal return at the k^{th} cell given that a certain n^{th} cell has no return is given by

$$\rho_{k/\tilde{n}} = \frac{\rho_k}{1 - \rho_n}, \quad \forall\, k, n \in \{N\}, k \neq n. \tag{6}$$

The aforementioned probabilities in the signal space will be incorporated into the design of the detectors and the evaluation of their performance in the next sections.

III. OCCLUSION-INFORMED DETECTOR DESIGN

In this section, we will present two formulations of the detection problem under the assumption of full occlusion across a group of cells. First, we will frame the problem as a multiple-hypothesis testing scenario, in line with our assumption that a single target return is expected in all cells. Second, we will approach the problem as a binary hypothesis testing situation at the CUT, taking into account the signal distribution in the other cells. In both cases, we will develop the MAP and ML detectors. The MAP detector assumes that knowledge of the probability model and values is available and utilizes this information for detection. In contrast, the ML detector lacks such knowledge and assumes equal probabilities of events [33].

A. MULTIPLE HYPOTHESIS TESTING DESIGN

Casting the problem as an M-ary detection problem is supposed to be a closer match under the assumption of full occlusion where we expect a single echo return in one of N cells in the range profile. Accordingly, we consider $M = N + 1$ hypotheses over the entire group of cells modeled as

$$\mathcal{H}_k : \mathbf{x}_{\{N\}} = \boldsymbol{\mu}_k + \mathbf{w}_{\{N\}} \quad \forall\, k \in \{N\} \tag{7}$$

where $\mathbf{x}_{\{N\}}$ is the stacked vector of all the processed signals at the group of N cells, $\mathbf{w}_{\{N\}}$ is a stacked vector of the noise, and $\boldsymbol{\mu}_k$ is a vector of size $LN \times 1$ defined as

$$\begin{aligned} \boldsymbol{\mu}_k &= [\mathbf{0}_L^T \ldots \mathbf{s}_k^T \ldots \mathbf{0}_L^T]^T \quad \forall\, k \in \{N\} \\ \boldsymbol{\mu}_k &= \mathbf{0}_{LN} \qquad\qquad\qquad\quad k = 0 \end{aligned} \tag{8}$$

where $L = N_{tx}\, N_{rx}$. The construction of $\boldsymbol{\mu}_k$ in (8) for $k \neq 0$ ensures that it contains zero elements everywhere except for elements with indices in the range of $[L(k-1)+1, Lk]$ that are populated by $\mathbf{s}_k$, where $\mathbf{s}_k = \alpha_k \mathbf{s}$, and $\mathbf{s}$ is the normalized steering vector towards the k^{th} cell. Please note that we have dropped the dependence on θ_k and ϕ_k. This is due to our assumption that the group of mutually occluding cells lies at the same azimuth and elevation angle.

By considering the signal space probabilities defined in (4), the optimum decision rule which minimizes the average error probability is the one that decides that $\mathbf{x}_{\{N\}}$ is generated according to $\mathcal{H}_k$ if $\rho_k p(\mathbf{x}_{\{N\}}|\mathcal{H}_k) = \max_j\{\rho_j\ p(\mathbf{x}_{\{N\}}|\mathcal{H}_j)\}$ [33].

Recalling the Gaussian PDF notation $e_{\sigma^2}(\mathbf{x}, \boldsymbol{\mu})$, the hypotheses formulation in (7) leads to the following likelihood:

$$p\left(\mathbf{x}_{\{N\}}|\mathcal{H}_k\right) = \zeta e_{\sigma_{\mathbf{w}}^2}\left(\mathbf{x}_{\{N\}}, \boldsymbol{\mu}_k\right), \tag{9}$$

where $\zeta = 1/(\pi^{LN} det(\sigma_{\mathbf{w}}^2 \mathbf{I}_{LN}))$. This likelihood can be simplified based on the signal model (1) as

$$p\left(\mathbf{x}_{\{N\}} \mid \mathcal{H}_k\right) = \begin{cases} \zeta e_{\sigma_{\mathbf{w}}^2}\left(\mathbf{x}_{\{\bar{N}\}}, \mathbf{0}_{L(N-1)}\right) & \text{for } k = 0 \\ \zeta e_{\sigma_{\mathbf{w}}^2}\left(\mathbf{x}_{\{\bar{N}\}}, \mathbf{0}_{L(N-1)}\right) & \\ \quad \times \exp\left(\frac{2\Re\{\mathbf{s}_k^H \mathbf{x}_k\} - \mathbf{s}_k^H \mathbf{s}_k}{\sigma_{\mathbf{w}}^2}\right) & \text{for } k \in \{N\} \end{cases} \tag{10}$$

Accordingly, the optimum M-ary MAP detector under full occlusion formulation is the following

$$\begin{aligned} &\text{Decide } \mathcal{H}_k \text{ if } \Gamma_k^{\text{MAP}} = \max_j\{\Gamma_j^{\text{MAP}}\} \quad \forall\, j \in \{\{N\}, 0\} \\ &\text{where} \\ &\Gamma_j^{\text{MAP}} = \rho_j\ p\left(\mathbf{x}_{\{N\}}|\mathcal{H}_j\right) / e_{\sigma_{\mathbf{w}}^2}\left(\mathbf{x}_{\{\bar{N}\}}, \mathbf{0}_{L(N-1)}\right). \end{aligned} \tag{11}$$

The test (11) assumes the knowledge of the mean of signals $\mathbf{s}_j = \alpha_j \mathbf{s}$ where is $\mathbf{s}$ is the known steering vector and α_j is the target's RCS, often unknown. In this context, the corresponding Generalized Likelihood Ratio Test (GLRT) detector is used wherein $\hat{\alpha}_j$ is estimated for each cell through Maximum Likelihood Estimation (MLE) of the likelihood functions under each hypothesis $\mathcal{H}_j$. The estimation results in $\hat{\alpha}_j = \mathbf{s}^H \mathbf{x}_j$ leading to $\hat{\mathbf{s}}_j = \mathbf{s}^H \mathbf{x}_j \mathbf{s}$ and a corresponding GLRT detector $\Gamma_j^{\text{MAP}} = \rho_j \exp(|\mathbf{s}^H \mathbf{x}_j|^2/\sigma_{\mathbf{w}}^2)$ for $j = 1, \ldots, N$.

The ML equivalent detector is obtained by assuming equal probabilities of signal returns at all cells, namely, $\rho_j = \rho_i\ \forall j, i \in \{N\}, j \neq i$. This simply translates to the following decision rule

$$\begin{aligned} &\text{Decide } \mathcal{H}_k \text{ if } \Gamma_k^{\text{ML}} = \max_j\{\Gamma_j^{\text{ML}}\} \quad \forall\, j \in \{\{N\}, 0\} \\ &\text{where} \\ &\Gamma_j^{\text{ML}} = \begin{cases} 1 & j = 0 \\ \exp\left(|\mathbf{s}^H \mathbf{x}_j|^2/\sigma_{\mathbf{w}}^2\right) & j \in \{N\}. \end{cases} \end{aligned} \tag{12}$$

Note that in both (11) and (12), the noise power $\sigma_{\mathbf{w}}^2$ is assumed to be known, which is typically estimated using secondary cells in practice. Moreover, from (12), it is evident that the resulting ML detector is equivalent to implementing a classic square law detector on the signal after angle match filtering at each cell. It then decides on the target presence at the cell with the maximum value of the test among all the cells related to the same range profile. Consequently, to maintain a certain probability of false alarms, the maximum value of the tests can be then compared against a threshold to decide either target presence in the corresponding cell or $\mathcal{H}_0$.

Moreover, while these detectors can enhance the detection performance under the full occlusion model, deciding strictly for a single hypothesis over the entire group of cells inherently imposes an upper bound on the probability of detection less than unity regardless of the probability of false alarms that can be tolerated. This is because a wrong decision here does not mean only a false alarm, but also a missed detection. The upper bound on the probability of detection of the ML version (12) is derived analytically in Appendix A and given by (27). From now on, we will refer to these detectors as the MAX detectors.

B. BINARY HYPOTHESIS TESTING DESIGN

In this section, we approach the detector design problem through binary hypothesis testing, where tests are formulated for each cell by considering the distribution of the processed signal across all the N cells within the same range profile. First, let us start by defining the simple binary hypothesis without occlusion modeling for an arbitrary cell k. The range processed signal under $\mathcal{H}_0$ and $\mathcal{H}_1$ can be expressed as:

$$\begin{cases} \mathcal{H}_1 : \mathbf{x}_k = \alpha_k \mathbf{s} + \mathbf{w}_k \\ \mathcal{H}_0 : \mathbf{x}_k = \mathbf{w}_k \end{cases} \tag{13}$$

This formulation leads to the classical GLRT detector:

$$\exp\left(\frac{|\mathbf{s}^H \mathbf{x}_k|^2}{\sigma_{\mathbf{w}}^2}\right) \underset{\mathcal{H}_0}{\overset{\mathcal{H}_1}{\gtrless}} \eta. \tag{14}$$

Now, we formulate the signal model under both hypotheses given the assumption of full occlusion across the range profile containing N cells. To account for signals from cells other than the CUT, we introduce a superscript n indicating the index of the CUT. Specifically, $\mathcal{H}_1^{(n)}$ and $\mathcal{H}_0^{(n)}$ represent the alternative and null hypotheses, respectively, when the n^{th} cell is the CUT. Thus, the detection problem under occlusion can be framed as testing the following hypotheses:

$$\begin{cases} \mathcal{H}_1^{(n)} : (\mathbf{x}_n = \mathbf{s}_n + \mathbf{w},\ \mathbf{x}_k = \mathbf{w}) \quad \forall\, k \in \{N\} \setminus n \\ \mathcal{H}_0^{(n)} : \begin{cases} (\mathbf{x}_n = \mathbf{w},\ \mathbf{x}_k = \mathbf{w}) \quad \forall\, k \in \{N\} \setminus n \\ (\text{OR}) \\ \left(\mathbf{x}_n = \mathbf{w},\ \mathbf{x}_k = \mathbf{w},\ \mathbf{x}_j = \mathbf{s}_j + \mathbf{w}\right) \\ \quad \text{for } j \in \{N\} \setminus n,\ \forall\, k \in \{N\} \setminus \{n, j\} \end{cases} \end{cases} \tag{15}$$

The formulation above indicates that under the alternative hypothesis, the CUT contains a signal due to the presence of a target at that cell, while all the other $N-1$ cells will only contain noise. Conversely, under the null hypothesis, the CUT contains only noise, while all the other cells may also contain only noise, or at most one of them may contain a target obstructing the signal of potential targets in other cells, including the CUT.

To derive the detector based on the above formulation, we need to express the likelihoods under each of the hypotheses. Let $\mathbf{x}_{\{\bar{N}\}}$ represent the stacked measurements of the signal related to all cells other than the CUT, where $\{\bar{N}\} := \{N\} \setminus n$, and the size of this set is $N-1$. Therefore, the likelihood under the alternative hypothesis can be formulated as follows:

$$p\left(\mathbf{x}_n | \mathcal{H}_1^{(n)}\right) = p\left(\mathbf{x}_n = \mathbf{s}_n + \mathbf{w}, \mathbf{x}_{\{\bar{N}\}} = \mathbf{w}_{\{\bar{N}\}}\right), \tag{16}$$

where $\mathbf{w}_{\{\bar{N}\}}$ is the stacked vector of all $(N-1)$ vectors modeling the noise at the cells other than CUT distributed as $\mathbf{w}_{\{\bar{N}\}} \sim \mathcal{CN}(0, \sigma_{\mathbf{w}}^2 \mathbf{I}_{L(N-1)})$. Consequently, (16) can be expressed as

$$p\left(\mathbf{x}_n | \mathcal{H}_1^{(n)}\right) = \zeta\, e_{\sigma_{\mathbf{w}}^2}(\mathbf{x}_n, \mathbf{s}_n) \cdot e_{\sigma_{\mathbf{w}}^2}\left(\mathbf{x}_{\{\bar{N}\}}, \mathbf{0}_{L(N-1)}\right) \tag{17}$$

where $\zeta = 1/(\pi^{LN} det(\sigma_{\mathbf{w}}^2 \mathbf{I}_{LN}))$.

Similarly, the likelihood under the null hypothesis can be expressed as:

$$\begin{aligned} p\left(\mathbf{x}_n | \mathcal{H}_0^{(n)}\right) = p\big(\mathbf{x}_n = \mathbf{w}, \big[&\mathbf{x}_{\{\bar{N}\}} = \mathbf{w}\ (\text{OR}) \\ &\mathbf{x}_{\{\bar{N}\}} = \boldsymbol{\mu}_1 + \mathbf{w}\ (\text{OR}) \ldots \\ &\mathbf{x}_{\{\bar{N}\}} = \boldsymbol{\mu}_N + \mathbf{w}\big]\big), \end{aligned} \tag{18}$$

where $\boldsymbol{\mu}_k$ is as defined in (8). The likelihood in (18) is the joint probability density function of the vector $\mathbf{x}_n$ given it contains noise only and the stacked vector $\mathbf{x}_{\{\bar{N}\}}$ modeled as a Gaussian mixture of signals with the different means $\boldsymbol{\mu}_k$ weighted by the probabilities of signal returns at the k^{th} cell defined in (6). Consequently, (18) can be written as:

$$p\left(\mathbf{x}_n | \mathcal{H}_0^{(n)}\right) = \zeta\, e_{\sigma_{\mathbf{w}}^2}(\mathbf{x}_n, \mathbf{0}_L) \cdot \sum_{\substack{k=0 \\ k \neq n}}^{N} \rho_{k/\tilde{n}}\, e_{\sigma_{\mathbf{w}}^2}\left(\mathbf{x}_{\{\bar{N}\}}, \boldsymbol{\mu}_k\right). \tag{19}$$

Using the likelihoods obtained in (16), and (18), we derive the detector which is characterized by testing the likelihood ratio Λ of the signal in the CUT given the signals of all other $\bar{N}$ cells against a threshold η as follows:

$$\Lambda(\mathbf{x}_n | \mathbf{x}_{\{\bar{N}\}}) = \frac{p\left(\mathbf{x}_n | \mathcal{H}_1^{(n)}\right)}{p\left(\mathbf{x}_n | \mathcal{H}_0^{(n)}\right)} \underset{\mathcal{H}_0^{(n)}}{\overset{\mathcal{H}_1^{(n)}}{\gtrless}} \eta \tag{20}$$

By plugging (17) and (18) into (20), the ratio test $\Lambda(\mathbf{x}_n | \mathbf{x}_{\{\bar{N}\}})$ becomes

$$\begin{aligned} \Lambda(\mathbf{x}_n | \mathbf{x}_{\{\bar{N}\}}) &= \frac{e_{\sigma_{\mathbf{w}}^2}(\mathbf{x}_n, \mathbf{s}_n) \cdot e_{\sigma_{\mathbf{w}}^2}\left(\mathbf{x}_{\{\bar{N}\}}, \mathbf{0}_{L(N-1)}\right)}{e_{\sigma_{\mathbf{w}}^2}(\mathbf{x}_n, \mathbf{0}_L) \cdot \sum_{\substack{k=0 \\ k \neq n}}^{N} \rho_{k/\tilde{n}}\, e_{\sigma_{\mathbf{w}}^2}\left(\mathbf{x}_{\{\bar{N}\}}, \boldsymbol{\mu}_k\right)} \\ &= \frac{e_{\sigma_{\mathbf{w}}^2}(\mathbf{x}_n, \mathbf{s}_n) \cdot e_{\sigma_{\mathbf{w}}^2}\left(\mathbf{x}_{\{\bar{N}\}}, \mathbf{0}_{L(N-1)}\right)}{e_{\sigma_{\mathbf{w}}^2}(\mathbf{x}_n, \mathbf{s}_n) \cdot e_{\sigma_{\mathbf{w}}^2}\left(\mathbf{x}_{\{\bar{N}\}}, \mathbf{0}_{L(N-1)}\right)} \\ &\quad \times \frac{\exp\left(\frac{2\Re\{\mathbf{s}_n^H \mathbf{x}_n\} - \mathbf{s}_n^H \mathbf{s}_n}{\sigma_{\mathbf{w}}^2}\right)}{\left[\rho_{0/\tilde{n}} + \sum_{\substack{k=1 \\ k \neq n}}^{N} \rho_{k/\tilde{n}} \exp\left(\frac{(2\Re\{\mathbf{s}_k^H \mathbf{x}_k\} - \mathbf{s}_k^H \mathbf{s}_k)}{\sigma_{\mathbf{w}}^2}\right)\right]} \end{aligned}$$

$$= \frac{\exp\left(\frac{2\Re\{\mathbf{s}_n^H\mathbf{x}_n\}-\mathbf{s}_n^H\mathbf{s}_n}{\sigma_{\mathbf{w}}^2}\right)}{\left[\rho_{0/\tilde{n}} + \sum_{\substack{k=1\\k\neq n}}^{N} \rho_{k/\tilde{n}} \exp\left(\frac{(2\Re\{\mathbf{s}_k^H\mathbf{x}_k\}-\mathbf{s}_k^H\mathbf{s}_k)}{\sigma_{\mathbf{w}}^2}\right)\right]} \tag{21}$$

Accordingly, this test is the optimum MAP test given that we know the probabilities $\rho_{k|\tilde{n}}$ and α_n. Assuming the former are known, the latter can be estimated through MLE as discussed in the previous section. By substituting the MLE estimate in (21), the attained detector (20) is

$$\Lambda^{\text{MAP}}(\mathbf{x}_n|\mathbf{x}_{\{\tilde{N}\}}) = \frac{\exp\left(\frac{|\mathbf{s}^H\mathbf{x}_n|^2}{\sigma_{\mathbf{w}}^2}\right)}{\rho_{0/\tilde{n}} + \sum_{\substack{k=1\\k\neq n}}^{N} \rho_{k/\tilde{n}} \exp\left(\frac{|\mathbf{s}^H\mathbf{x}_k|^2}{\sigma_{\mathbf{w}}^2}\right)} \underset{\mathcal{H}_0^{(n)}}{\overset{\mathcal{H}_1^{(n)}}{\gtrless}} \eta \tag{22}$$

Note that in (22), we have assumed that the noise power $\sigma_{\mathbf{w}}^2$ is known, which is typically estimated using secondary cells in practice. The selection of cells suitable for noise estimation can be further explored in an extended version of this work.

The corresponding ML detector can be obtained by assuming equal probabilities of return at all cells, with $\rho_{k/\tilde{n}}\ \forall k \in \{N\}$, and is given by:

$$\Lambda^{\text{ML}}(\mathbf{x}_n|\mathbf{x}_{\{\tilde{N}\}}) = \frac{\exp\left(\frac{|\mathbf{s}^H\mathbf{x}_n|^2}{\sigma_{\mathbf{w}}^2}\right)}{\frac{1}{N}\left[1 + \sum_{\substack{k=1\\k\neq n}}^{N} \exp\left(\frac{|\mathbf{s}^H\mathbf{x}_k|^2}{\sigma_{\mathbf{w}}^2}\right)\right]} \underset{\mathcal{H}_0^{(n)}}{\overset{\mathcal{H}_1^{(n)}}{\gtrless}} \eta. \tag{23}$$

Accordingly, the resulting tests in (22) and (23) suggest that the optimal detectors under the full occlusion assumption correspond to the classic test performed at the CUT (13), normalized by a weighted sum of the tests from other cells within the same range profile.

The detectors derived in Sections III-A and III-B are specifically designed for scenarios involving full occlusion. Unlike a classical detector that considers only the signal in the CUT, the proposed detectors also account for signals in other cells across the entire range profile containing the CUT. This incurs slightly more computational complexity. Assuming a constant complexity for the exponential and squared law operators, the classical detector performs $O(N)$ comparisons against a threshold for N cells. In contrast, the Max-ML detector (12) performs a max operation and one comparison, resulting in $O(N+1)$ complexity. The Binary-ML detector (23) involves N additions for each cell plus one comparison and one division, leading to a complexity of $O(N^2+2)$. This increase in complexity is justified by the significantly higher detection performance in full occlusion scenarios, as will be shown in the numerical analysis.

IV. NUMERICAL ANALYSIS

In this section, we evaluate the performance of the proposed detectors on two fronts. Firstly, we model the signal after the angle processing block as input to the detector, employing the full occlusion model presented earlier. We demonstrate the performance of the derived detectors through ROC curves and compare them with the classic detector. Secondly, we simulate a real indoor scenario observed with a Frequency Modulated Continuous Wave (FMCW) system operating in the mmWave band. This system is equipped with multiple transmitting and receiving antennas operating in a Time Division Multiplexing (TDM) scheme, thereby realizing a MIMO radar system. Unlike the model-based case, scenario-based simulations consider the complete standard signal processing chain, starting from the reflected signal and concluding with the detection stage. We then compare the output of the detectors accordingly.

A. MODEL-BASED ROC ASSESSMENT

Here, we evaluate the proposed detectors by numerical analysis using Monte Carlo simulations. We demonstrate the performance of these proposed detectors through ROC curves. The detectors are implemented on a set of N test cells, assumed to mutually occlude under a full occlusion scenario. Given this assumption, signal returns are generated so that in each realization, only one out of the N cells contains a target return. The presence or absence of a return at each cell follows a particular signal space probability model, derived from the assumed probability model in the target space, as described in (4). Throughout the various Monte Carlo realizations, two sets of signals are generated to represent the null and alternative hypotheses at a predefined CUT. Subsequently, the different detectors are applied, and ROC curves are constructed by sorting the test output relative to each hypothesis and calculating the corresponding probability of false alarm and probability of detection.

To illustrate the signal generation process based on a specific probability model, Fig. 3 presents an example of probabilities in the target space P_k (a) and signal space ρ_k (b) at each cell, along with the corresponding events of signal returns under the null and alternative hypotheses in (c) and (d), respectively. For enhanced visualization, consider this as a simplified example, with a limited number of Monte Carlo runs ($K_{MC} = 10^3$) and a small range profile size of $N = 32$ cells. In this particular example, the probability model for target presence follows a linearly increasing pattern, with the lowest probability assigned to the cell closest to the sensor and the highest to the farthest cell, set at 0.25. Additionally, CUT is arbitrarily selected as cell index $n = 23$, indicated by a cross in (a) and (b), and outlined by a red rectangle in (c) and (d).

As shown in the figure, the chosen probability model in the target space leads to a higher probability of returns in the signal space for cells located in the middle. In our analysis, we considered two probability models additionally: one with an equal probability of target presence at all cells and another with a linearly decreasing model where the closest cell has the highest probability of target presence. Under each probability model, ranges of the maximum probability of the target's presence in a cell are evaluated.

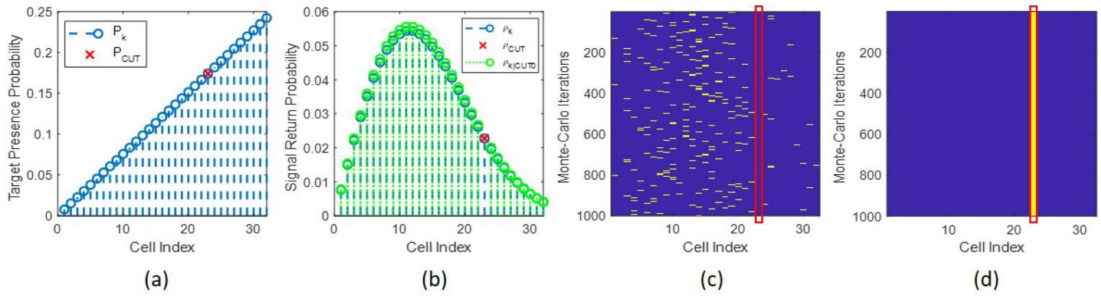

FIGURE 3. Illustration of signal generation in all cells under null and alternative hypotheses for a certain CUT n (highlighted with the red rectangle) given a probability model in the target space for $N = 32$, $n = 23$, $K_{MC} = 10^3$. (a) Probabilities of targets presence P_k, (b) Probabilities of receiving a signal return (marginal ρ_k, and conditioned on no return in CUT $\rho_{k|\bar{n}}$), (c) Monte-Carlo realizations of signal return events under $\mathcal{H}_0^{(n)}$, and (d) Monte-Carlo realizations of signal return events under $\mathcal{H}_1^{(n)}$.

We evaluate the performance of the MAP and ML detectors derived according to binary and multiple hypothesis testing, presented in (11), (12), (22), and (23). All our subsequent simulations entail $K_{MC} = 10^8$ Monte Carlo runs for robust assessment. Comparisons are made against the classic detector (14). Fig. 4 showcases this assessment when a fixed SNR of 10 dB is maintained at the CUT, and for a range profile size of $N = 128$. The columns represent different probability models–equal probabilities, linearly increasing, and decreasing probabilities–while rows denote varying maximum probabilities of target presence in a cell $(P_k)_{\max} = (0.1, 0.5, \text{and } 0.9)$ from top to bottom. From the figure, several key observations emerge:

- Detectors derived from binary hypothesis formulation under full occlusion consistently outperform the classic detector.
- The MAX detector shows superior detection capability up to a certain probability of false alarm. However, its performance saturates beyond this threshold due to the non-linear maximum operator, particularly noticeable in low SNR scenarios.
- The performance of MAP detectors is scenario-dependent and therefore would lack the constant false alarm rate (CFAR) property.
- MAP detectors demonstrate maximum performance improvement when closer cells have a higher probability of target presence, suggesting a greater likelihood of occlusion for more distant targets.
- While the highest performance gain is provided by binary MAP detectors, the corresponding ML detector still consistently outperforms the classic detector.

Building on the observations mentioned earlier, our subsequent analysis narrows down to the performance evaluation of ML detectors, given their practical applicability. This analysis seeks to assess their performance concerning the size of the range profile N and the SNR levels.

In Fig. 5, we observe the performance of the detectors across different numbers of mutually occluding cells, specifically $N = 16, 32, 64,$ and 128, assessed at SNR levels of 8, 10, and 13 dB. The figure highlights that the detection performance gain is significant with a lower number of occluding cells. Additionally, it demonstrates a decrease in the upper-bound probability of detection for the MAX detector as N increases, especially noticeable at low SNR levels. However, at high SNR levels, the performance gain difference diminishes, with gains of approximately 10% achieved at a false alarm probability of 10^{-6} for an SNR level of 13 dB.

Likewise, Fig. 6 depicts the detector's performance as SNR varies across different values of N. It becomes evident that the higher the SNR, the more significant the gain of ML detectors compared to the classic one. Moreover, at high SNR values, the MAX detector achieves a higher detection probability bound, but this decreases significantly at low SNR levels, rendering its use unfeasible.

B. SCENARIO-BASED SIMULATIONS

In the previous section, we evaluated detectors' performance based on a defined signal model and specific parameters such as SNR, number of mutually occluding cells, and probability of target presence at individual range cells. This section presents a simulation of a dynamic indoor scenario where multiple human objects move within the scene along predetermined trajectories, resulting in various occlusions, including self-occlusions and inter-object occlusions. We observe this scenario using an FMCW radar sensor equipped with multiple antenna elements for both transmitting and receiving. We generate the radar signal based on a ray-tracing algorithm in tandem with the system parameters. Following this, we process the received signal through a typical radar signal processing chain. After range and angle processing, we apply the classic detector, the detector from (23) (abbreviated as Occ-ML), and that from (12) (abbreviated as Max-ML), and subsequently compare their performance. In the following subsections, we will elaborate on the modeling of the scenario and targets, the radar signal generation and processing, and finally, the evaluation of the proposed detectors against a classic detector.

1) SCENARIO DESCRIPTION AND MODELLING

We consider a scenario where five human targets are walking in an indoor environment along different trajectories. The scenario is designed using 3D models of actual-size human

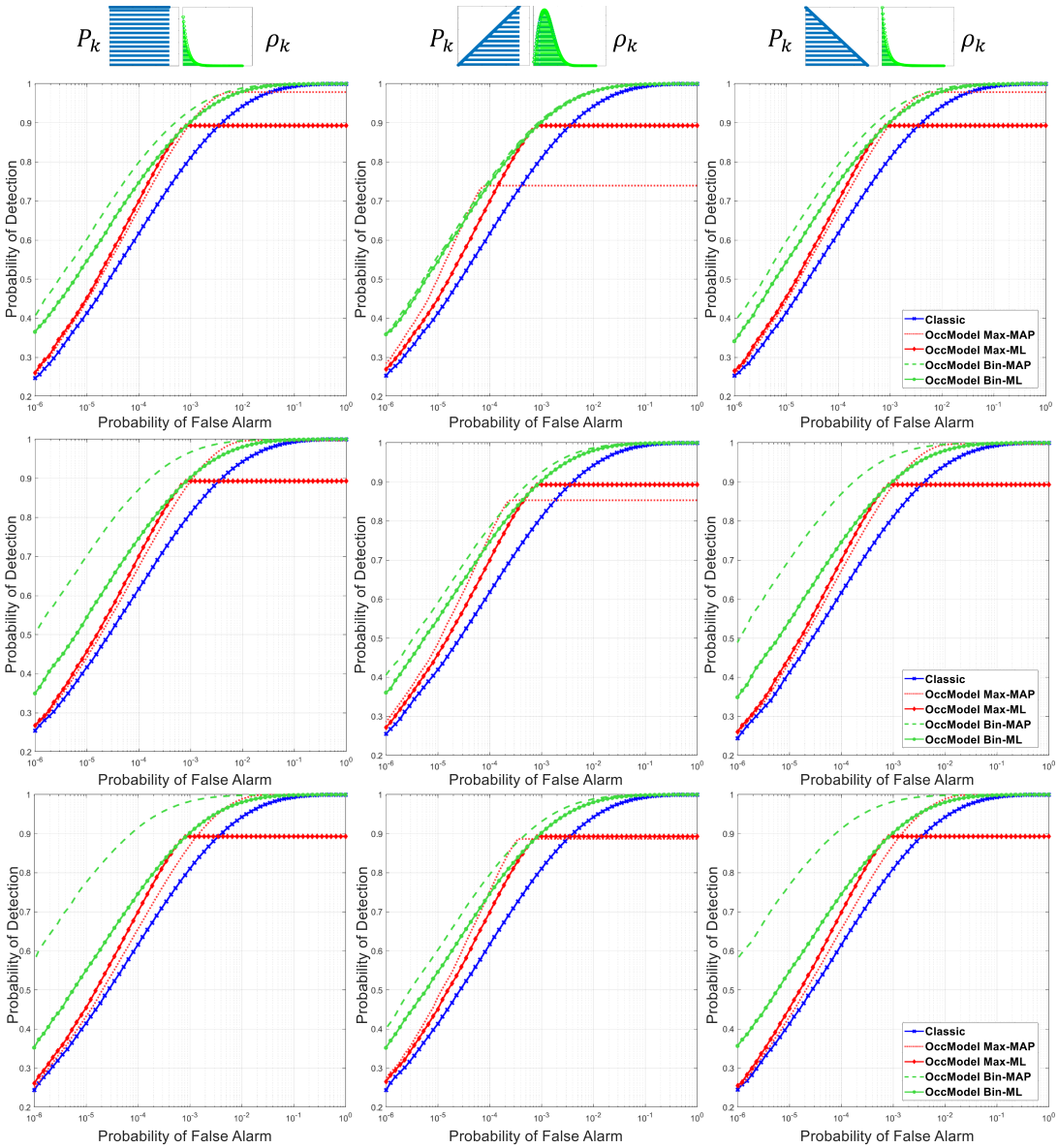

FIGURE 4. **ROC curves of proposed detectors compared against classic detector for $N = 128$ cells and SNR $= 10$ dB, for different models of the probability of targets arrival in resolution cells and different values of maximum probability of target presence p_{max} at cells. Left column: equal probability, Middle column: linearly increasing, Right column: linearly decreasing. Top row: $p_{max} = 0.1$, Middle row: $p_{max} = 0.5$, Bottom row: $p_{max} = 0.9$.**

objects animated in Blender software [34]. Spanning five seconds at a frame rate of 20 frames/second, it results in a total of 100 graphical frames. Each 3D model consists of a high-resolution mesh of many constituent triangle batches, resulting in an average triangle surface area of 0.001 m^2. These triangle batches serve as scattering surfaces, defined by an origin vector and two side vectors. Consequently, we utilize a ray-tracing algorithm to identify triangles that have a Line of Sight (LOS) with respect to each transmitting/receiving antenna pair and to quantify the reflected rays. The primary objective of radar ray-tracing is to determine the ray paths from the transmitter to the receiver antenna elements and calculate their amplitude and distance, essential for the generation of the radar signal.

Ray-casting is the fundamental operation employed in ray tracing, involving the calculation of ray-triangle intersections. When a ray intersects a triangle, an intersection point is identified, leading to the generation of new rays for the next bounce. Accordingly, ray tracing starts by assigning rays to each transmit antenna element, calculating intersections with the triangles (if any), and assigning new ray sources for each of the intersection points. Subsequently, the new rays are bounced back in some directions, and a new path is established for the rays that have a LOS intersecting with the receiving antenna.

Consequently, the algorithm outputs a set of rays for each triangle with respect to each transmit and receive antenna pair. The length of each ray represents the relative travel distance of

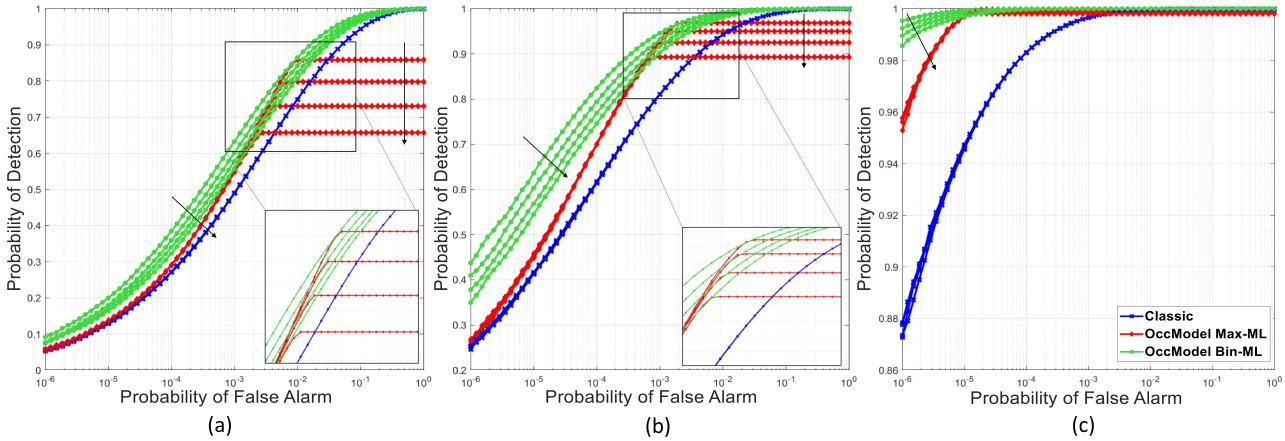

FIGURE 5. ROC curves of proposed ML occlusion-informed detectors compared to classic detector varying the number of mutually occluding cells $N = 16, 32, 64, 128$ (the arrows indicate the direction of increasing N) at different SNR levels. (a) 8 dB, (b) 10 dB, and (c) 13 dB.

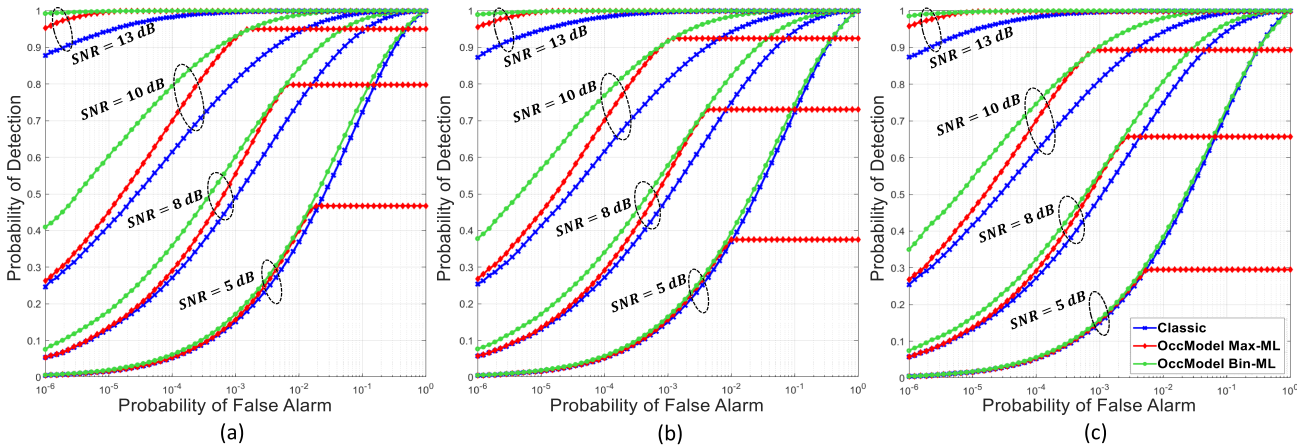

FIGURE 6. ROC curves of proposed ML occlusion-informed detectors compared to classic detector varying SNR at different numbers of mutually occluding cells. (a) $N = 32$, (b) $N = 64$, and (c) $N = 128$.

the transmitted electromagnetic wave, reflecting off the target and reaching the receiving antenna element. Meanwhile, the amplitude of the scattered radar wave is determined by the radar equation considering the RCS of the triangle and the corresponding path length to account for attenuation. Ideally, the RCS calculation should account for the number of reflected rays from each triangle, its surface orientation relative to the transmit/receive element pair, and the Normalized RCS [35] given the surface's material. For simplicity, we modeled the RCS of each triangle based on the relative aspect angles (azimuth and elevation) of its normal vector from the origin point, modulating a maximum preset RCS value $\sigma_{\max} = 0.01$ m^2. Fig. 7 shows a snapshot of a single time frame depicting the human 3D models and the constituent triangle meshes in (b), highlighting the origin points of the triangles with LOS with respect to the antenna configuration of the sensor located at the $y-z$ plane with its center placed at coordinates $(0, 0, 1)$ (a), and a close-up to one of the human objects for enhanced visualization in (c).

TABLE 1. FMCW Radar System Parameters

Central Frequency (f_c)	70 (GHz)
Effective Sweeping Bandwidth (BW)	1 (GHz)
Effective Chirp Duration (T_{chirp})	5.124 (µs)
ADC Sampling Frequency (f_s)	2.5 (MHz)
Transmitter Power (p_{Tx})	13 (dBm)
Receiver Noise Figure (F)	12 (dB)
Number of TX Elements (N_{Tx})	121
Number of RX Elements (N_{Rx})	121

2) RADAR SIGNAL GENERATION

We employ an FMCW MIMO radar sensor operating in a TDM fashion to observe the described scenario. The operating parameters and sensor characteristics for generating the radar signal are detailed in Table 1. As shown in Fig. 7(a), the sensor comprises a 121-element transmitting planar array with an inter-element spacing of $11\lambda/2$, and a 121-element planar receiving array spaced at $\lambda/2$. By assigning each element of the transmitting array to transmit at different time slots, a

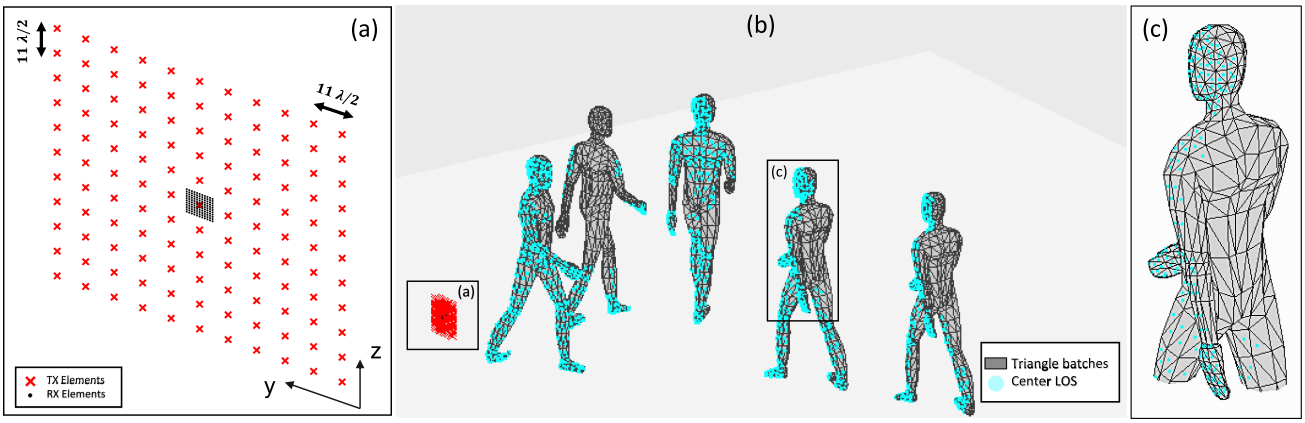

FIGURE 7. Simulation scenario and modeling. (a) Configuration of 121 × 121 TX-RX antennas for the radar sensor. (b) Snapshot of a single time frame of the scenario depicting human targets modeled using triangle batches, highlighting the origin points of triangle batches with LOS. (c) Close-up view of a single human object.

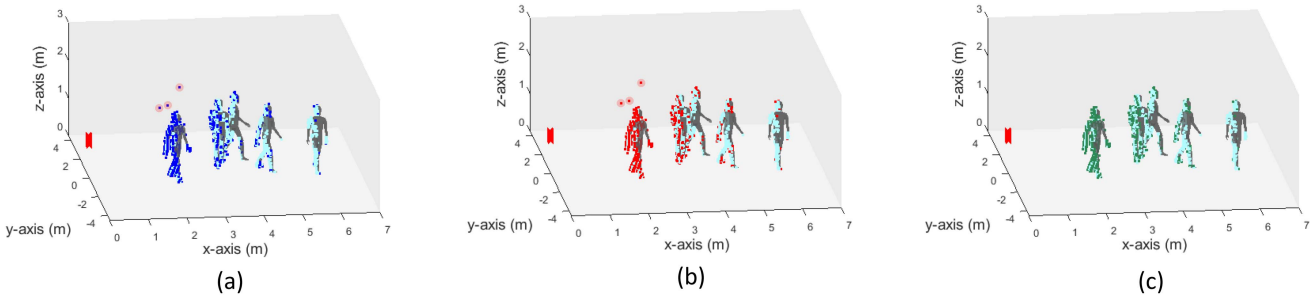

FIGURE 8. Single time frame snapshot of point cloud detection highlighting some of the visible false alarms of Classic and Max-ML detectors not present in the output of Occ-ML detector. (a) Classic detector output (b) Max-ML detector output (c) Occ-ML detector output.

resulting uniform planar virtual array is achieved leading to an angular resolution of approximately 1.165° in both azimuth and elevation. This low angular resolution promotes cell-level occlusion, thereby encouraging the application of our derived detector as it assumes that each resolution cell encompasses a limited scattering area, resulting in one or few backscattered echoes over a certain range profile.

Accordingly, we simulate the sampled received Intermediate Frequency (IF) signal (indexed by time samples n_s) at each receiving antenna (n_{RX}), resulting from a backscattered wave due to the signal transmitted by the n_{TX} element, as follows:

$$y(n_s, n_{Tx}, n_{Rx}) = \sum_{r=1}^{N_{rays}} A(p_{Tx}, d_r, \sigma_r) \cdot [\exp(-j2\pi(\mu\tau n_s/f_s + f_c\tau n_s/f_s)) \cdot \exp(\mathbf{k}(\theta_r, \phi_r)^T(\mathbf{r}_{n_{Tx}} + \mathbf{r}_{n_{Rx}}))]. \quad (24)$$

Here, N_{rays} represents the total number of rays traced from the transmitter element to the scene and back to the receiver element. $A(.)$ denotes the amplitude of the scattered wave which depends on the transmitted power p_{TX}, the two-way length of a ray d_r, and the associated triangle RCS σ_r. Additionally, $\mu = BW/T_c$ denotes the slope of the chirp, while $\tau = d_r/c$ is the associated time delay and c is the speed of light in vacuum. Finally, $\mathbf{k}$ is the wave number defined in Section II, θ_r and ϕ_r are the relative azimuth and elevation angles of the normal vector of the surface associated with the traced ray with respect to the sensor, respectively, and $\mathbf{r}_{n_{Tx}}$ and $\mathbf{r}_{n_{Rx}}$ are the coordinate vectors of the transmitting and receiving antenna elements, respectively.

Consequently, for each graphical frame, we have 121 × 121 channels, each having a $N_s = T_{chirp}f_s = 128$ time samples. The simulated raw data is then organized in a 2D matrix, with the time samples at the first dimension and the channel data at the second dimension. Lastly, we add the thermal noise to all the channels as a white Gaussian noise with power $p_{noise} = (k_B\ T\ BW\ F)$, where k_B is Boltzmann constant, T is the absolute room temperature, and F is the receiver noise figure.

3) RADAR SIGNAL PROCESSING

To process the radar signal, we begin by acquiring the 2D matrix of the raw signal at each frame. We then proceed with a standard signal processing chain, involving range FFT and

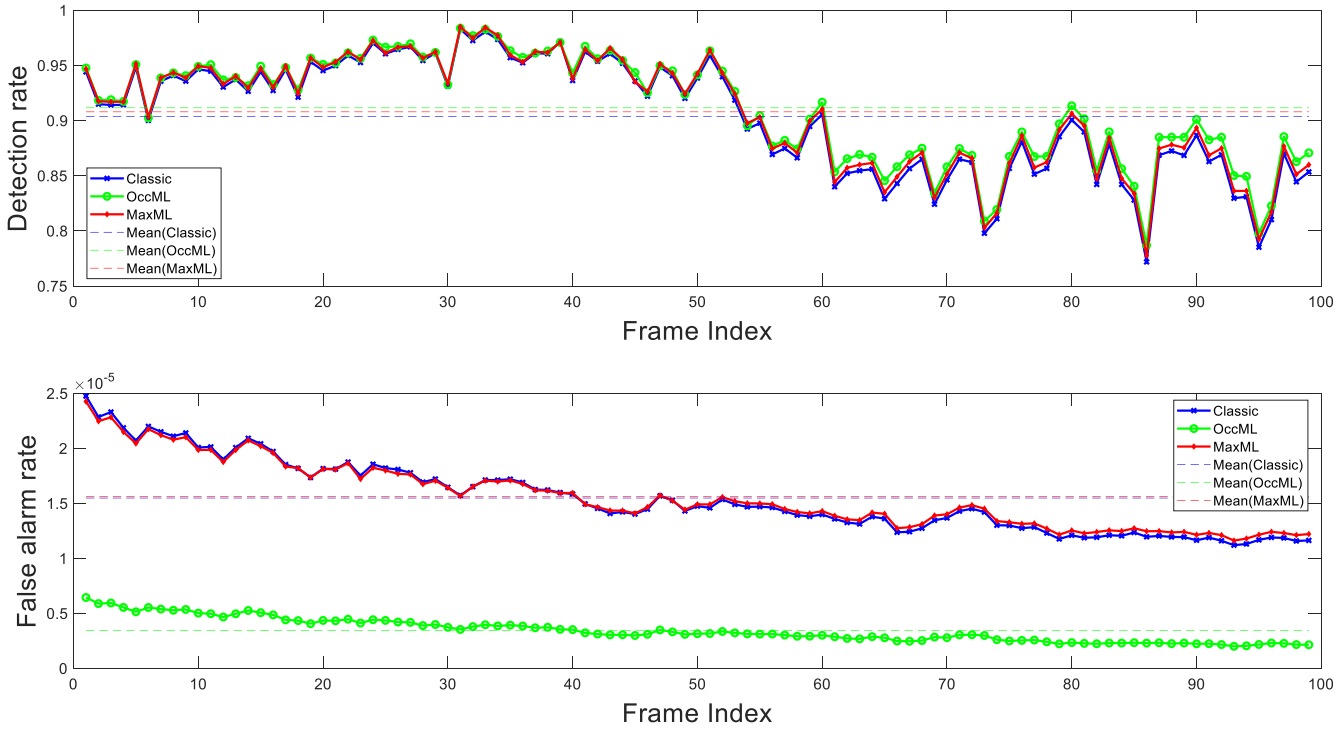

FIGURE 9. Detection performance versus time frames. **Top:** Detection rate. **Bottom:** False alarms rate.

angle processing using steering vectors. Finally, the detection performance of the three detectors needs to be compared. Initially, we apply the range FFT on the first dimension of the raw data matrix, choosing the grid size to be a power of two that yields a size of half of the range resolution offered by the system's bandwidth.

Subsequently, angle processing is conducted over a Field of View (FOV) of 160° on the azimuth dimension and 70° in elevation. These FOVs were chosen to reduce computational complexity, considering the dimensions of the observed scene. The number of angular bins in azimuth and elevation is similarly set to achieve a grid step size that is half of the angular resolution in both dimensions. Angle processed signal is acquired by multiplying each channel by the corresponding steering vector, as defined in (2), for all the angles within the FOVs.

After angle processing, we apply the tests outlined in Section III to each range profile, along with a classic test simplified to a square-law detector. To determine the threshold corresponding to the desired probability of false alarms, we utilize Cell-Averaging (CA)-CFAR to estimate the local noise level at each CUT from neighboring secondary cells. Anticipating superior performance of the OCC-ML detector based on ROC curves from the previous section, we set a lower required probability of false alarms (PFA) for the CFAR applied after this specific test. Fig. 8 shows a snapshot of the detection output for the three detectors at a specific time frame, illustrating the lower false alarm rate set for the Occ-ML detector while demonstrating that the correct detection points are nearly identical. A numerical evaluation of the detection performance for the three detectors is provided in the following subsection. The parameters used for the different processing blocks are summarized in Table 2.

TABLE 2. Radar Signal Processing and Detection Parameters

Number of Range FFT Bins	256
Number of Azimuth Bins	275
Number of Elevation Bins	121
CA-CFAR PFA (Classic/Max) Detector	10^{-6}
CA-CFAR PFA (OccML) Detector	10^{-7}
CA-CFAR number of training cells	12
CA-CFAR number of guard cells	2

4) PERFORMANCE EVALUATION

To assess the performance of different implemented detectors, we establish a ground truth grid for each frame. The ground truth grid matches the size of the range-angle grid of the processed signal and has entries of one at the cells that correspond to the location of origin of triangles with LOS rays. Similarly, we construct a grid for each detector, where the locations of detected targets are also marked as one. Subsequently, performance is evaluated by computing the detection rate (DR) and false alarm rate (FR) using the following formulas:

$$DR = \frac{TP}{TP + FN}, \quad FR = \frac{FP}{FP + TN}, \tag{25}$$

where TP, FN, FP, and TN represent the counts of true positives, false negatives, false positives, and true negatives, respectively. These values are calculated with respect to the

obtained ground truth grid over 30 Monte Carlo runs of different noise realizations. The values of DR and FR versus frame are illustrated in Fig. 9.

The figure shows that the detection rate of all three detectors remains nearly equal across all frames, despite the OccML detector being configured to achieve a lower false alarm rate which is achieved consistently. This performance aligns with the analytical analysis presented in Section IV-A. It is important to highlight that the analytical model-based simulations were conducted for specific SNR values, demonstrating varying performance at each value. In contrast, in this realistic scenario-based simulation, each target has a different SNR level that also changes over time, still, the OccML detector exhibits superior performance. On the other hand, the Max detector does not consistently improve detection performance on average. This observation aligns with the findings from the ROC curves presented in the model-based analysis. For certain SNR values and ranges of PFA values, the MaxML detector outperforms the classic detector, whereas for other SNR values and PFA ranges, the opposite holds true. Additionally, even though the assumption of a single echo per range profile might not hold for all range profiles, on average, the proposed OccML detector enhances detection performance.

V. CONCLUSION

In this paper, we introduced a novel approach to enhance the detection capabilities of mmWave MIMO sensors with high angular resolution capability, particularly in indoor environments. We achieve this by leveraging the sparsity of range profiles under occlusion scenarios where, among multiple targets that exist on a specific angular bin, the sensor only receives the signal reflected from one target occluding all the others. By utilizing this structure, we proposed two detection methods based on two formulations: multiple hypothesis testing and binary hypothesis testing to enhance the detection of non-occluded targets under these scenarios.

Our numerical evaluations demonstrated that, for a low required probability of false alarm, all the proposed methods outperformed a classic detector which does not account for this sparse structure, providing a higher probability of detection. However, at higher probabilities of false alarms, especially in low SNR scenarios, detectors derived from multiple hypotheses exhibited an upper limit on the probability of detection that could not be exceeded. In contrast, detectors based on our binary hypothesis formulation significantly outperformed the classic detector, especially when knowledge of the probability model and target presence values in the cells was available. While obtaining such knowledge is often impractical and parameter-dependent, the ML binary detector, while providing a slightly lower gain than its MAP counterpart, consistently outperformed the classic detector under all probability models. We further demonstrated the performance of the proposed detectors on realistically simulated data for an indoor scenario where the radar signal is generated using ray tracing and the full standard signal processing chain is applied to the received radar signal.

Future works may include: formulating similar approaches for occlusion scenarios where range profiles show lower sparsity due to targets partially occupying cells, devising methods for sensors to recognize occlusion scenarios and transition from being informed to being aware, and advancing fusion techniques for detection across multiple sensors by integrating insights from occlusion-informed/aware approaches.

APPENDIX A
DERIVATION OF THE UPPER BOUND ON P_D OF MAX-ML DETECTOR

The Max-ML detector decides $\mathcal{H}_k$ if:

$$\Gamma_k^{\mathrm{ML}} = \max_j \{\Gamma_j^{\mathrm{ML}}\} \quad \forall\, j \in \{\{N\}, 0\}.$$

Assuming the correct hypothesis is $\mathcal{H}_m$, the maximum attainable P_D is:

$$\begin{aligned} P_D &\leqslant \Pr\left[\Gamma_m^{\mathrm{ML}} > \Gamma_j^{\mathrm{ML}}, \forall\, j \in \{\bar{N}\} \mid \mathcal{H}_m\right] \\ &\leqslant \Pr\left[\exp\left(|\mathbf{s}^H \mathbf{x}_m|^2/\sigma_{\mathbf{w}}^2\right) > \exp\left(|\mathbf{s}^H \mathbf{x}_j|^2/\sigma_{\mathbf{w}}^2\right) \mid \mathcal{H}_m\right], \end{aligned}$$

where $\{\bar{N}\} := \{N\} \setminus m$. For simplicity, consider a scalar signal at each cell ($\mathbf{s} = 1, \mathbf{x}_k \in \mathbb{C}^{1\times 1}$). The generalization to the vector signal is straightforward since the resulting bound will be expressed in terms of SNR and the inner product in the vector case introduces a gain in the SNR equals to $(N_{tx} \times N_{rx})$. Accordingly, assuming equal probability of the M hypotheses, the upper bound in this case is:

$$\begin{aligned} P_D &\leqslant \Pr\left[\exp\left(\frac{|x_m|^2}{\sigma_w^2}\right) > \exp\left(\frac{|x_j|^2}{\sigma_w^2}\right), \forall\, j \in \{\bar{N}\} \mid \mathcal{H}_m\right] \\ &\leqslant \Pr\left[\left(\frac{|x_m|^2}{\sigma_w^2}\right) - \left(\frac{|x_j|^2}{\sigma_w^2}\right) > 0, \forall\, j \in \{\bar{N}\} \mid \mathcal{H}_m\right] \end{aligned}$$

where under $\mathcal{H}_m$:

$$\begin{cases} x_m \sim \mathcal{CN}\left(\alpha_m, \sigma_w^2\right) \\ x_j \sim \mathcal{CN}\left(0, \sigma_w^2\right) \end{cases}$$

Let us denote with Z, Y, and R the following random variables

$$\begin{aligned} Z &= |x_m|^2/(\sigma_w^2/2) \\ Y &= -\max\{|x_j|^2/(\sigma_w^2/2)\}, \qquad j \in \{\bar{N}\} \\ R &= Z + Y \end{aligned}$$

Thus,

$$P_D \leqslant \Pr\left[Z + Y > 0\right] = \Pr\left[R > 0\right] = \int_0^\infty p_R(r)dr$$

The PDF of R is the convolution of the PDFs of Z and Y, given by

$$\begin{aligned} p_Z(z) &= \frac{1}{2}\exp\left(-\frac{(z+\lambda)}{2}\right) I_0(\sqrt{\lambda z}), \quad z \geqslant 0 \\ p_Y(y) &= \frac{(N-1)}{2}\exp\left(\frac{y}{2}\right)\left(1 - \exp\left(\frac{y}{2}\right)\right)^{N-2}, \quad y \leqslant 0 \end{aligned}$$

where I_0 is the modified Bessel function of the first kind and $\lambda = 2\alpha_m^2/\sigma_w^2$, which is twice the SNR of the signal at the m^{th} cell. Accordingly, the $p_R(r)$ can be obtained as:

$$p_R(r) = \begin{cases} \int_0^\infty p_z(z)p_y(r-z)dz & r \leqslant 0 \\ \int_r^\infty p_z(z)p_y(r-z)dz & r > 0 \end{cases} \tag{26}$$

Let I denote the indefinite integral form of the PDF, then

$$\begin{aligned} I &= \int p_z(z)p_y(r-z)dz \\ &= \int \left(\frac{N-1}{4}\right) \exp\left(\frac{-(z+\lambda)}{2}\right) I_0(\sqrt{\lambda z}) \\ &\quad \times \exp\left(\frac{r-z}{2}\right)\left(1-\exp\left(\frac{r-z}{2}\right)\right)^{N-2} dz \\ &= \frac{(N-1)}{4}\exp\left(\frac{r-\lambda}{2}\right)\int \exp(-z) I_0(\sqrt{\lambda z})dz \\ &\quad \times \left(1-\exp\left(\frac{r-z}{2}\right)\right)^{N-2} dz \end{aligned}$$

The term $(1-\exp(\frac{r-z}{2}))^{N-2}$ can be expanded using the binomial theorem as

$$\left(1-\exp\left(\frac{r-z}{2}\right)\right)^{N-2} = \sum_{k=0}^{N-2}\binom{N-2}{k}(-1)^k \exp\left(\frac{kr-kz}{2}\right)$$

Consequently,

$$\begin{aligned} I &= \frac{(N-1)}{4}\exp\left(\frac{r-\lambda}{2}\right)\sum_{k=0}^{N-2}\binom{N-2}{k}(-1)^k \exp\left(\frac{kr}{2}\right) \\ &\quad \times \int \exp\left(\frac{-(k+2)}{2}z\right) I_0(\sqrt{\lambda z})dz \end{aligned}$$

The integral has a known solution over 0 to ∞ [36]. Plugging in the solution, we obtain $p_R(r)$ over its negative support:

$$\begin{aligned} p_R(r) &= \frac{(N-1)}{4}\exp\left(\frac{r-\lambda}{2}\right)\sum_{k=0}^{N-2}\binom{N-2}{k}(-1)^k \exp\left(\frac{kr}{2}\right) \\ &\quad \times \int_0^\infty \exp\left(-z-\frac{kz}{2}\right) I_0(\sqrt{\lambda z})dz \\ &= \frac{(N-1)}{4}\exp\left(\frac{r-\lambda}{2}\right)\sum_{k=0}^{N-2}\binom{N-2}{k}(-1)^k \exp\left(\frac{kr}{2}\right) \\ &\quad \times \left(\frac{2}{k+2}\right)\exp\left(\frac{\lambda}{2(k+2)}\right), \quad r \leqslant 0 \end{aligned}$$

Finally, the upper bound on P_D under the Max-ML detector is given by

$$\begin{aligned} P_D &\leqslant \int_0^\infty p_R(r)dr = 1 - \int_{-\infty}^0 p_R(r)dr \\ &\leqslant 1 - \left[\frac{(N-1)}{4}\exp\left(\frac{-\lambda}{2}\right)\sum_{k=0}^{N-2}\binom{N-2}{k}(-1)^k \left(\frac{2}{k+2}\right)\right. \\ &\quad \left.\times \exp\left(\frac{\lambda}{2(k+2)}\right)\int_{-\infty}^0 \exp\left(\frac{r+kr}{2}\right)dr\right] \\ &\leqslant 1 - \left[\frac{(N-1)}{4}\exp\left(\frac{-\lambda}{2}\right)\sum_{k=0}^{N-2}\binom{N-2}{k}(-1)^k \right. \\ &\quad \left.\left(\frac{2}{k+2}\right)\times \exp\left(\frac{\lambda}{2(k+2)}\right)\left(\frac{2}{k+1}\right)\right]. \end{aligned} \tag{27}$$

ACKNOWLEDGMENT

The authors would like to thank Johann Fuchs for his assistance in generating the 3D indoor scenario in Blender. This research was funded in whole, or in part, by the Luxembourg National Research Fund (FNR), grant reference [IF/15364040/RADII]. For the purpose of open access, and in fulfillment of the obligations arising from the grant agreement, the author has applied a Creative Commons Attribution 4.0 International (CC BY 4.0) license to any Author Accepted Manuscript version arising from this submission.

REFERENCES

[1] Y. Kim and T. Moon, "Human detection and activity classification based on micro-Doppler signatures using deep convolutional neural networks," *IEEE Geosci. Remote Sens. Lett.*, vol. 13, no. 1, pp. 8–12, Jan. 2016.

[2] G. Beltrão et al., "Contactless radar-based breathing monitoring of premature infants in the neonatal intensive care unit," *Sci. Rep.*, vol. 12, no. 1, 2022, Art. no. 5150.

[3] B. Erol, M. G. Amin, and B. Boashash, "Range-Doppler radar sensor fusion for fall detection," in *Proc. 2017 IEEE Radar Conf. (RadarConf)*, 2017, pp. 819–824.

[4] H. Cui and N. Dahnoun, "High precision human detection and tracking using millimeter-wave radars," *IEEE Aerosp. Electron. Syst. Mag.*, vol. 36, no. 1, pp. 22–32, Jan. 2021.

[5] "mmWave radar sensors TI.com." Accessed: Sep. 13, 2023. [Online]. Available: https://www.ti.com/sensors/mmwave-radar/overview.html

[6] "NXP introduces advanced automotive radar one-chip family for next-GEN ADAS and autonomous driving systems." Accessed: Sep. 13, 2023. [Online]. Available: https://www.nxp.com/company/about-nxp/nxp-introduces-advanced-automotive-radar-one-chip-family-for-next-gen-adas-and-autonomous-driving-systems:nw-nxp-introduces-advanced-automotive-radar-one

[7] A. Bourdoux, U. Ahmad, D. Guermandi, S. Brebels, A. Dewilde, and W. Van Thillo, "PMCW waveform and MIMO technique for a 79 GHz CMOS automotive radar," in *Proc. 2016 IEEE Radar Conf.*, 2016, pp. 1–5.

[8] E. Raei, M. Alaee-Kerahroodi, P. Babu, and M. R. B. Shankar, "Generalized waveform design for sidelobe reduction in MIMO radar systems," *Signal Process.*, vol. 206, 2023, Art. no. 108914, doi: 10.1016/j.sigpro.2022.108914.

[9] M. Alaee-Kerahroodi, P. Babu, M. Soltanalian, and B. S. Maysore Rama Rao, *Signal Design for Modern Radar Systems*. Norwood, MA, USA: Artech House, 2022.

[10] N. K. Sichani, M. Alaee-Kerahroodi, B. S. Maysore Rama Rao, E. Mehrshahi, and S. A. Ghorashi, "Antenna array and waveform design for 4D-imaging mmWave MIMO radar sensors," *IEEE Trans. Aerosp. Electron. Syst.*, vol. 60, no. 2, pp. 1848–1864, Apr. 2024.

[11] S. Z. Gürbüz, C. Clemente, A. Balleri, and J. J. Soraghan, "Micro-Doppler-based in-home aided and unaided walking recognition with multiple radar and sonar systems," *IET Radar Sonar Navigation*, vol. 11, pp. 107–115, 2017, doi: 10.1049/iet-rsn.2016.0055.

[12] Z. Yang, P. H. Pathak, Y. Zeng, X. Liran, and P. Mohapatra, "Vital sign and sleep monitoring using millimeter wave," *ACM Trans. Sensor Netw.*, vol. 13, no. 2, pp. 14:1–14:32, 2017.

[13] M. Shen, K.-L. Tsui, M. A. Nussbaum, S. Kim, and F. Lure, "An indoor fall monitoring system: Robust, multistatic radar sensing and explainable, feature-resonated deep neural network," *IEEE J. Biomed. Health Inform.*, vol. 27, no. 4, pp. 1891–1902, Apr. 2023.

[14] J. Pegoraro and M. Rossi, "Real-time people tracking and identification from sparse mm-Wave radar point-clouds," *IEEE Access*, vol. 9, pp. 78504–78520, 2021.

[15] A. Palffy, J. F. P. Kooij, and D. M. Gavrila, "Detecting darting out pedestrians with occlusion aware sensor fusion of radar and stereo camera," *IEEE Trans. Intell. Veh.*, vol. 8, no. 2, pp. 1459–1472, Feb. 2023.

[16] S. K. Kwon, E. Hyun, J.-H. Lee, J. Lee, and S. H. Son, "Detection scheme for a partially occluded pedestrian based on occluded depth in LiDAR–radar sensor fusion," *Opt. Eng.*, vol. 56, no. 11, 2017, Art. no. 113112.

[17] V. Chernyak, "Multisite radar systems composed of MIMO radars," *IEEE Aerosp. Electron. Syst. Mag.*, vol. 29, no. 12, pp. 28–37, Dec. 2014.

[18] E. Fishler, A. Haimovich, R. Blum, L. Cimini, D. Chizhik, and R. Valenzuela, "Spatial diversity in radars–models and detection performance," *IEEE Trans. Signal Process.*, vol. 54, no. 3, pp. 823–838, Mar. 2006.

[19] M. Ahmadi, M. Alaee-Kerahroodi, B. S. Maysore Rama Rao, and B. Ottersten, "Subspace-based detector for distributed mmWave MIMO radar sensors," in *Proc. 2023 IEEE Int. Conf. Acoust. Speech Signal Process.*, 2023, pp. 1–5.

[20] A. Murtada, B. S. Maysore Rama Rao, and U. Schroeder, "GLRT detector for aspect-dependent fluctuating targets using distributed mmWave MIMO radar sensors," in *Proc. IEEE 2023 31st Eur. Signal Process. Conf.*, 2023, pp. 1574–1578.

[21] M. Canil, J. Pegoraro, A. Shastri, P. Casari, and M. Rossi, "ORACLE: Occlusion-resilient and self-calibrating mmWave radar network for people tracking," *IEEE Sensors J.*, vol. 24, no. 3, pp. 3157–3171, Feb. 2024.

[22] A. Shastri, M. Canil, J. Pegoraro, P. Casari, and M. Rossi, "mmSCALE: Self-calibration of mmWave radar networks from human movement trajectories," in *Proc. 2022 IEEE Radar Conf.*, 2022, pp. 1–6.

[23] T. Yang, J. Cao, and Y. Guo, "Placement selection of millimeter wave FMCW radar for indoor fall detection," in *Proc.2018 IEEE MTT-S Int. Wireless Symp.*, 2018, pp. 1–3.

[24] D. Liu, U. S. Kamilov, and P. T. Boufounos, "Sparsity-driven distributed array imaging," in *Proc. 2015 IEEE 6th Int. Workshop Comput. Adv. Multi-Sensor Adaptive Process.*, 2015, pp. 441–444.

[25] V. H. Tang, A. Bouzerdoum, and S. L. Phung, "Compressive radar imaging of stationary indoor targets with low-rank plus jointly sparse and total variation regularizations," *IEEE Trans. Image Process.*, vol. 29, pp. 4598–4613, 2020.

[26] T. Benoudiba-Campanini, J.-F. Giovannelli, and P. Minvielle, "SPRITE: 3-D sparse radar imaging technique," *IEEE Trans. Comput. Imag.*, vol. 6, pp. 1059–1069, 2020.

[27] R. Hu, B. S. Maysore Rama Rao, A. Murtada, M. Alaee-Kerahroodi, and B. Ottersten, "Widely-distributed radar imaging based on consensus ADMM," in *Proc. 2021 IEEE Radar Conf.*, 2021, pp. 1–6.

[28] D. Kozlov and P. Ott, "CFAR detector for compressed sensing radar based on l1-norm minimisation," in *Proc. IEEE 2020 28th Eur. Signal Process. Conf.*, 2021, pp. 2050–2054.

[29] C. A. Rogers and D. C. Popescu, "Compressed sensing MIMO radar system for extended target detection," *IEEE Syst. J.*, vol. 15, no. 1, pp. 1381–1389, Mar. 2021.

[30] J. Ding, M. Wang, H. Kang, and Z. Wang, "MIMO radar super-resolution imaging based on reconstruction of the measurement matrix of compressed sensing," *IEEE Geosci. Remote Sens. Lett.*, vol. 19, 2022, Art. no. 3504705.

[31] M. Jafri, S. Srivastava, S. Anwer, and A. K. Jagannatham, "Sparse parameter estimation and imaging in mmWave MIMO radar systems with multiple stationary and mobile targets," *IEEE Access*, vol. 10, pp. 132836–132852, 2022.

[32] A. Murtada, R. Hu, B. S. Maysore Rama Rao, and U. Schroeder, "Widely distributed radar imaging: Unmediated ADMM based approach," *IEEE J. Sel. Topics Signal Process.*, vol. 17, no. 2, pp. 389–402, Mar. 2023.

[33] R. G. Gallager, *Stochastic Processes: Theory for Applications*, 1st ed. Cambridge, U.K.: Cambridge Univ. Press, 2013.

[34] "blender (3.6 LTS), blender foundation." Accessed: Feb. 11, 2024. [Online]. Available: https://www.blender.org/download/

[35] C. Schüßler, M. Hoffmann, J. Bräunig, I. Ullmann, R. Ebelt, and M. Vossiek, "A realistic radar ray tracing simulator for large MIMO-arrays in automotive environments," *IEEE J. Microw.*, vol. 1, no. 4, pp. 962–974, Oct. 2021.

[36] "DLMF: 10.43 integrals modified bessel functions chapter 10 bessel functions." Accessed: Jul. 22, 2024. [Online]. Available: https://dlmf.nist.gov/10.43